



Article

# Preparation of a Z-Type g-C<sub>3</sub>N<sub>4</sub>/(A-R)TiO<sub>2</sub> Composite Catalyst and Its Mechanism for Degradation of Gaseous and Liquid Ammonia

Jiaming Zhu <sup>1,2</sup> , Zuohua Liu <sup>1</sup>, Hao Wang <sup>1,2</sup>, Yue Jian <sup>1,2</sup>, Dingbiao Long <sup>1,2,\*</sup> and Shihua Pu <sup>1,2,\*</sup>

<sup>1</sup> Chongqing Academy of Animal Sciences, Chongqing 402460, China

<sup>2</sup> Scientific Observation and Experiment Station of Livestock Equipment Engineering in Southwest, Ministry of Agriculture, Chongqing 402460, China

\* Correspondence: longdb@cqaa.cn (D.L.); push@cqaa.cn (S.P.)

**Abstract:** In this study, an (A-R)TiO<sub>2</sub> catalyst (ART) was prepared via the sol–gel method, and g-C<sub>3</sub>N<sub>4</sub> (CN) was used as an amendment to prepare the g-C<sub>3</sub>N<sub>4</sub>/(A-R)TiO<sub>2</sub> composite catalyst (ARTCN). X-ray diffraction (XRD), scanning electron microscopy (SEM), transmission electron microscopy (TEM), Raman spectroscopy, N<sub>2</sub> adsorption–desorption curves (BET), UV–Vis diffuse absorption spectroscopy (UV–Vis DRS), and fluorescence spectroscopy (PL) were used to evaluate the structure, morphology, specific surface area, optical properties, and photocarrier separation ability of the catalysts. The results showed that when the modifier CN content was 0.5 g, the dispersion of the ARTCN composite catalyst was better, with stronger light absorption performance, and the forbidden band width was smaller. Moreover, the photogenerated electrons in the conduction band of ART transferred to the valence band of CN and combined with the holes in the valence band of CN, forming Z-type heterostructures that significantly improved the efficiency of the photogenerated electron-hole migration and separation, thus increasing the reaction rate. Gaseous and liquid ammonia were used as the target pollutants to investigate the activity of the prepared catalysts, and the results showed that the air wetness and initial concentration of ammonia had a great influence on the degradation of gaseous ammonia. When the initial concentration of ammonia was 50 mg/m<sup>3</sup> and the flow rate of the moist air was 0.9 mL/min, the degradation rate of gaseous ammonia by ARTCN-0.5 reached 88.86%, and it had good repeatability. When the catalytic dose was 50 mg and the initial concentration of NH<sub>4</sub><sup>+</sup> was 100 mg/L, the degradation rate of liquid ammonia by ARTCN-0.5 was 71.60% after 3 h of reaction, and small amounts of NO<sub>3</sub><sup>−</sup> and NO<sub>2</sub><sup>−</sup> were generated. The superoxide anion radical (·O<sub>2</sub><sup>−</sup>) and hydroxyl radical (·OH) were the main active components in the photocatalytic reaction process.

**Keywords:** photocatalysis; ammonia; degradation; mechanism



**Citation:** Zhu, J.; Liu, Z.; Wang, H.; Jian, Y.; Long, D.; Pu, S. Preparation of a Z-Type g-C<sub>3</sub>N<sub>4</sub>/(A-R)TiO<sub>2</sub> Composite Catalyst and Its Mechanism for Degradation of Gaseous and Liquid Ammonia. *Int. J. Mol. Sci.* **2022**, *23*, 13131. <https://doi.org/10.3390/ijms232113131>

Academic Editor: Dippong Thomas

Received: 28 September 2022

Accepted: 26 October 2022

Published: 28 October 2022

**Publisher's Note:** MDPI stays neutral with regard to jurisdictional claims in published maps and institutional affiliations.



**Copyright:** © 2022 by the authors. Licensee MDPI, Basel, Switzerland. This article is an open access article distributed under the terms and conditions of the Creative Commons Attribution (CC BY) license (<https://creativecommons.org/licenses/by/4.0/>).

## 1. Introduction

Ammonia is a colorless alkaline gas that causes strong irritation, mainly from agricultural fertilization, animal husbandry, and the use of antifreeze [1]. Estimates have shown that China emits 10 to 15 million tons of ammonia into the air every year, almost double the total of the United States and the European Union [2]. Large-scale ammonia emissions will not only cause diseases in animals and humans, such as central muscle paralysis and bronchitis, but also cause global climate change [3]. Ammonia reacts with oxides in the air, producing particulate matter such as ammonium sulfate and ammonium nitrate, which are the main factors that form haze [4]; thus, controlling ammonia emissions is beneficial to controlling haze [5]. In addition, ammonia gas will return to the surface through atmospheric dry and wet deposition, leading to the eutrophication of water and affecting the stability of the ecosystem [6]. Traditional ammonia treatment processes have high costs and poor stability, which may aggravate the secondary pollution of the environment [7].

In 1972, Fujishima discovered that  $\text{TiO}_2$  could photolyze water under ultraviolet light, and this photocatalytic reaction has been widely used in environmental governance, energy development, biological applications, self-cleaning materials, antibacterial applications, sensors, and other fields due to its thorough reaction and lack of secondary pollution [8]. For example, A. Enesca et al. [9] prepared doped tin oxide films with different dopant concentrations through spray pyrolysis deposition and found that the photodegradation efficiency of the  $\text{SnO}_2$  film could reach about 30% under the condition of zinc doping. X. Hu et al. [10] introduced and discussed the current challenges and future development prospects of  $\text{CO}_2$  photoreduction for hydrocarbon fuels. X. Liu et al. [11] prepared  $\text{CdS@ZIS-SV}$ , and its hydrogen production rate reached 18.06 mmol/g/h, which was 16.9 and 19.6 times that of original  $\text{CdS}$  (1.16 mmol/g/h) and  $\text{ZIS}$  (0.92 mmol/g/h) materials, respectively. In ammonia gas degradation, P.A. Kolinko et al. [12] and H.M. Wu et al. [13] pointed out that the N element had various valence states. Herein, its main product was  $\text{N}_2$ , and its by-products were  $\text{N}_2\text{O}$ ,  $\text{NO}_2^-$ , and  $\text{NO}_3^-$ . Among the many photocatalytic materials,  $\text{TiO}_2$  has become photocatalyst with the most potential due to its advantages such as good chemical stability, safety, non-toxicity, low cost, and strong REDOX ability [14]. Most studies have indicated that the degradation performance of anatase (A- $\text{TiO}_2$ ) is better than rutile (R- $\text{TiO}_2$ ), and reports on  $\text{TiO}_2$  have mainly used the anatase phase [15]. Shen et al. [16] stated that when the A- $\text{TiO}_2$  and R- $\text{TiO}_2$  phases formed a heterogeneous structure, an internal electric field could form, thus promoting the transfer of charges on the interface and improving photocatalytic activity. Das et al. [17] prepared a mixed anatase/rutile crystal structure that had a higher photocatalytic performance than commercial P25 under visible light. Xiong et al. [18] showed that mixed crystalline anatase and rutile  $\text{TiO}_2$  nanoparticles exhibited a high photocatalytic carbon dioxide reduction capacity. However, its high bandgap width (3.2 eV for anatase and 3.0 eV for rutile) resulted in a response to only high-energy UV light, and its photogenerated charge carriers were easy to recombine, thus limiting its catalytic activity [19]. For example, Guarino et al. [20] sprayed  $\text{TiO}_2$  on a wall with a total area of 150 m<sup>2</sup> at a spray quantity of 70 g/m<sup>2</sup> and using a 36 W UV light as the light source, and the degradation rate of ammonia was found to be about 30%.

Photocatalytic materials can be used to form heterogeneous structures. For example, Shihua Pu et al. [21] achieved the degradation of ammonia under sunlight for the first time through the  $\text{Cu}_2\text{O}$  improvement of {001} $\text{TiO}_2$ , and the degradation rate of ammonia was found to be more than 80% within 2 h. However, due to the photocorrosion of  $\text{Cu}_2\text{O}$  itself, the degradation rate of ammonia gas was only maintained at 40% after four repeated uses, making the choice of amendment very important.  $g\text{-C}_3\text{N}_4$  has shown a narrow band gap, with a wide range of light responses and good thermal stability, chemical stability, and strong corrosion resistance [22]. Most studies have found that the formation of heterostructures through the preparation of  $g\text{-C}_3\text{N}_4/\text{TiO}_2$  composite catalysts could broaden the solar spectral response of the catalyst, and photogenerated charge carriers are not easy to recombine [23]. For example, Li et al. [24] constructed a  $g\text{-C}_3\text{N}_4/\text{TiO}_2$  heterostructure that achieved effective photoinduced electron-hole separation in the photocatalytic process and showed a good photocatalytic effect and cyclic stability. Zhao S et al. [25] used synthesized  $g\text{-C}_3\text{N}_4/\text{TiO}_2$  to degrade phenol with 2.41 and 3.12 times  $g\text{-C}_3\text{N}_4$  and  $\text{TiO}_2$  contents, respectively. Sun et al. [26] used synthetic  $g\text{-C}_3\text{N}_4/\text{TiO}_2$  to degrade methylene blue with 1.85 and 4 times pure  $g\text{-C}_3\text{N}_4$  and  $\text{TiO}_2$  content, respectively; this showed that it was feasible to improve  $\text{TiO}_2$  degradation capacity by using  $g\text{-C}_3\text{N}_4$  as an amendment, but a study on ammonia degradation has not been previously reported.

In this study, an (A-R) $\text{TiO}_2$  catalyst (ART) was prepared via the sol-gel method, where  $g\text{-C}_3\text{N}_4$  (CN) was used as an amendment to prepare  $g\text{-C}_3\text{N}_4/(\text{A-R})\text{TiO}_2$  (ARTCN) with a Z-type heterostructure, which improved the efficiency of photogenerated electron-hole migration and separation. In this study, using gaseous ammonia and ammonia as the target pollutants, we explored the ARTCN degradation of ammonia, the mechanism of performance improvement, the intermediate, and the reaction process. We also studied

the repeated use of ARTCN, as evidence on the properties and mechanism noted in this research regarding the effective governance of ammonia pollution has been relatively scarce, and this research could provide a certain theoretical basis for the management of ammonia.

## 2. Results

### 2.1. Analysis of the Characterization Results

#### 2.1.1. XRD Analysis

When  $2\theta = 25.28^\circ, 36.95^\circ, 37.80^\circ, 38.55^\circ, 48.04^\circ, 53.89^\circ, 55.06^\circ, 62.68^\circ, 70.31^\circ, 75.03^\circ,$  and  $76.02^\circ$ , the characteristic peaks corresponding to the (101), (103), (004), (112), (200), (105), (211), (204), (220), (215), and (301) crystal planes, respectively, were almost consistent with the anatase  $\text{TiO}_2$  (JCPDS No. 21-1272) standard cards [27]. Furthermore,  $2\theta = 27.45^\circ, 36.09^\circ, 39.19^\circ, 41.26^\circ, 44.05^\circ, 54.32^\circ, 56.64^\circ, 64.04^\circ,$  and  $69.01^\circ$  corresponded to the (110), (101), (200), (111), (210), (211), (220), (310), and (301) crystal planes, respectively, which was almost consistent with the rutile  $\text{TiO}_2$  (JCPDS No. 21-1276) standard card [28]. The characteristic peaks at  $2\theta = 13.1^\circ$  and  $27.5^\circ$  belonged to the (100) and (002) planes, respectively which was largely in line with  $g\text{-C}_3\text{N}_4$  (JCPDS87-1526) [29].

Figure 1 shows the XRD patterns of the prepared samples. We found that ART contained not only the characteristic peaks of the anatase phase but also the characteristic peaks of the rutile phase, indicating that it was a mixed crystal type, which was the prepared (A-R) $\text{TiO}_2$  catalyst. CN had a weak diffraction peak near  $13.1^\circ$ , corresponding to the (100) crystal plane of CN, which was formed by the 3-S monotriazine structural unit of the plane [30]. There was a strong diffraction peak at  $27.50^\circ$ , which was caused by the layered accumulation of graphite in the conjugate plane. The diffraction peak of the ARTCN-X composite corresponded to pure ART, which indicated that CN did not enter the ART lattice and was only attached to its surface. There was no diffraction peak in the composite samples of ART and CN at  $13.1^\circ$ , because the amount of CN was small and had a weak peak. Although the peaks of CN at  $27.50^\circ$  and R- $\text{TiO}_2$  at  $27.45^\circ$  coincided, we observed that as the composite ratio increased from 0.1 to 1, the composite gradually widened around  $27^\circ$ , indicating that the composite material was successfully prepared.

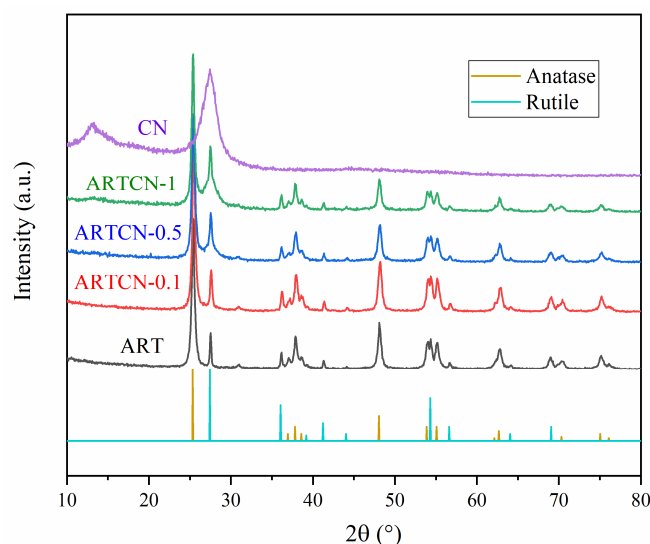


**Figure 1.** XRD patterns of the samples.

The accuracy was further verified by calculating the rutile content of several materials [31], and the calculation results are shown in Table 1. We found that the rutile contents of ART, ARTCN-0.1, ARTCN-0.5, and ARTCN-1 were 23.49%, 25.06%, 29.43%, and 34.61%, respectively. High temperatures were conducive to the conversion of A- $\text{TiO}_2$  into R- $\text{TiO}_2$ , while ART, ARTCN-0.1, ARTCN-0.5, and ARTCN-1 were prepared at the same tempera-

ture; thus, the increased rutile content was not rutile in the real sense but rather the added amendment of CN.

**Table 1.** Rutile content of the catalysts.

Samples	$I_R$ ( $2\theta = 27.24^\circ$ )	$I_A$ ( $2\theta = 25.28^\circ$ )	$X_R$
ART	523.48	2131.93	23.49%
ARTCN-0.1	605.19	2260.33	25.06%
ARTCN-0.5	704.02	2110.14	29.43%
ARTCN-1	953.81	2251.77	34.61%

Table 1 shows the rutile content of each catalyst. The formula (Equation (1)) is given as follows:

$$X_R = \frac{1}{1 + 0.8 \times \frac{I_A}{I_R}} \quad (1)$$

where  $X_R$  is the rutile content,  $I_A$  is the peak intensity of anatase at  $2\theta = 25.28^\circ$ , and  $I_R$  is the peak intensity of rutile at  $2\theta = 27.24^\circ$ .

### 2.1.2. Raman Analysis

The crystal form and structure of the catalyst were further determined by Raman spectroscopy, and Figure 2 shows the Raman spectra of the prepared catalyst. The anatase phase of  $\text{TiO}_2$  corresponded to  $\nu = 144 \text{ cm}^{-1}$ ,  $\nu = 197 \text{ cm}^{-1}$ ,  $\nu = 392 \text{ cm}^{-1}$ ,  $\nu = 514 \text{ cm}^{-1}$ , and  $\nu = 635 \text{ cm}^{-1}$  [32], while  $\nu = 437 \text{ cm}^{-1}$  corresponded to rutile  $\text{TiO}_2$ . The reason why other characteristic peaks did not appear was that the content of rutile in ART was low (as indicated by the peak intensity of XRD). ART and composite ARTCN-X both had anatase and rutile peaks, especially the CN peak of ARTCN-1, which further validated the XRD results.

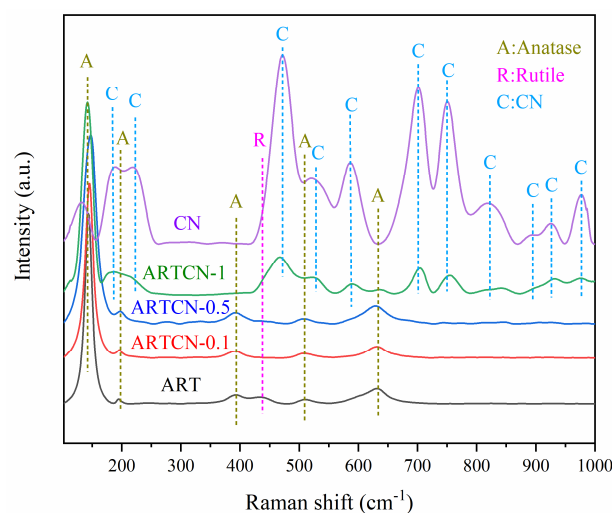


**Figure 2.** Raman spectra of the samples.

### 2.1.3. Morphology and Lattice Spacing Analysis

According to Figure 3a,h, CN was a curved and folded film with certain holes. As shown in Figure 3b,i, ART consisted of a particle with a uniform size but serious agglomeration, and Figure 3c shows that CN in ARTCN-0.5 was no longer a whole film but fragmented into many small pieces; thus, its position relative to ART could not be clearly observed. Combined with Figure 3d–g, we clearly observed that elements O, Ti, and N were evenly distributed in ARTCN-0.5. This showed that a composite material with a heterogeneous structure was synthesized. In addition, as clearly shown in Figure 3j, the ART agglomeration phenomenon was significantly improved after the improvement of

CN, which indicated that the utilization of light by ART in the composite ARTCN-0.5 was further enhanced.

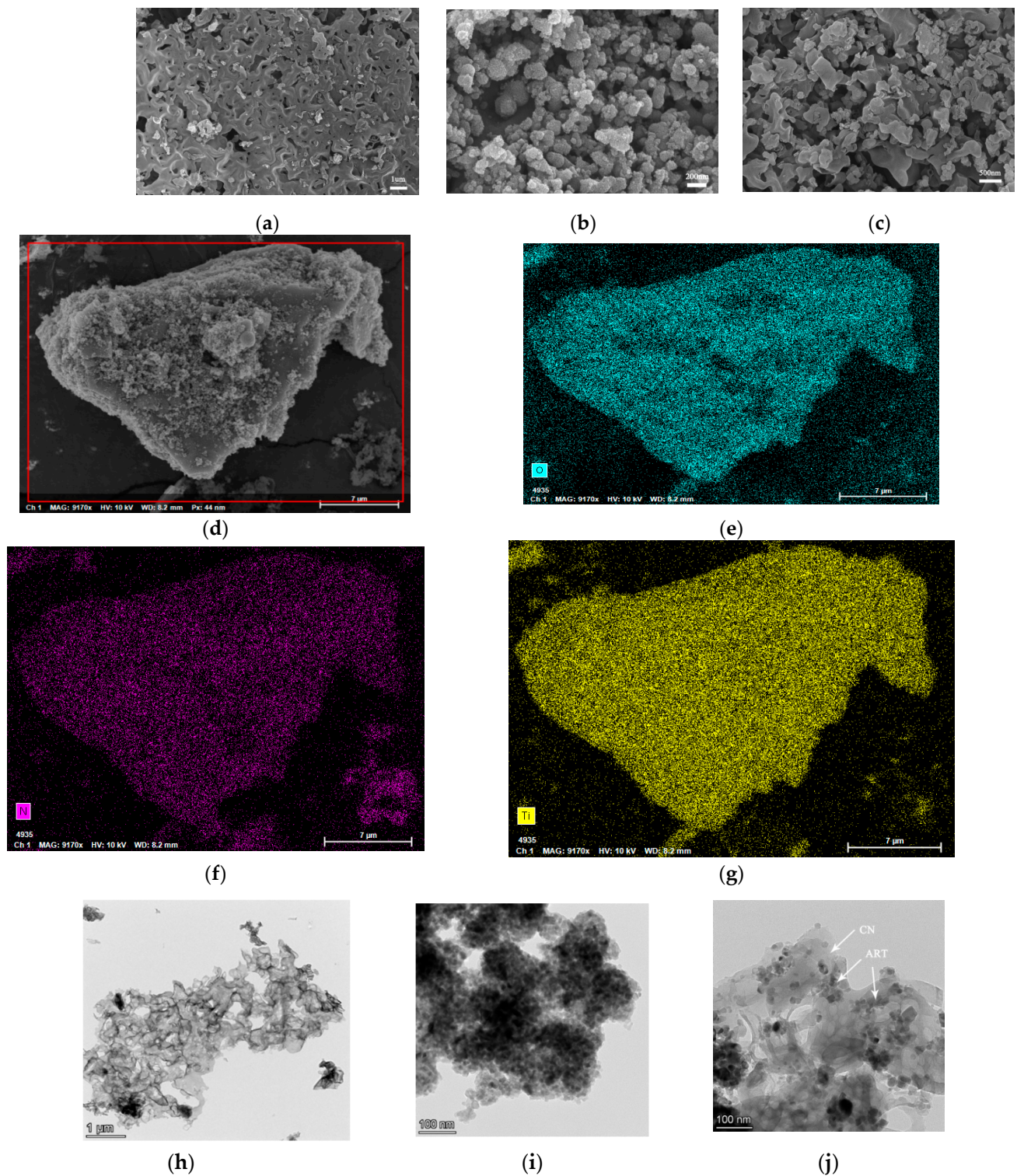


**Figure 3.** SEM images of CN (a), ART (b), and ARTCN-0.5 (c); images and corresponding EDS elemental mapping images (d–g) of the ARTCN-0.5, TEM of CN (h), ART (i), and ARTCN-0.5 (j).

#### 2.1.4. Analysis of Adsorption–Desorption of $N_2$

The Brunauer–Emmett–Teller (BET) method was used to calculate the surface area of the catalyst, and the Barrett–Joyner–Halenda (BJH) method was used to analyze the

pore size and pore volume. The catalysts shown in Figure 4a all exhibited typical nitrogen adsorption–desorption isotherms of type IV, and the hysteresis loops of the catalysts all showed obvious openings, indicating the formation of mesoporous catalysts [33]. Figure 4b shows the pore size distribution of the catalyst, which showed that the pore size of the prepared catalyst was mainly concentrated at 0–20 nm, indicating that the particle size distribution of the catalyst was narrow. Combined with the data in Table 2, we found that the pores of the catalysts showed little difference, while the specific surface area and pore diameter of the catalysts increased with increasing CN content.

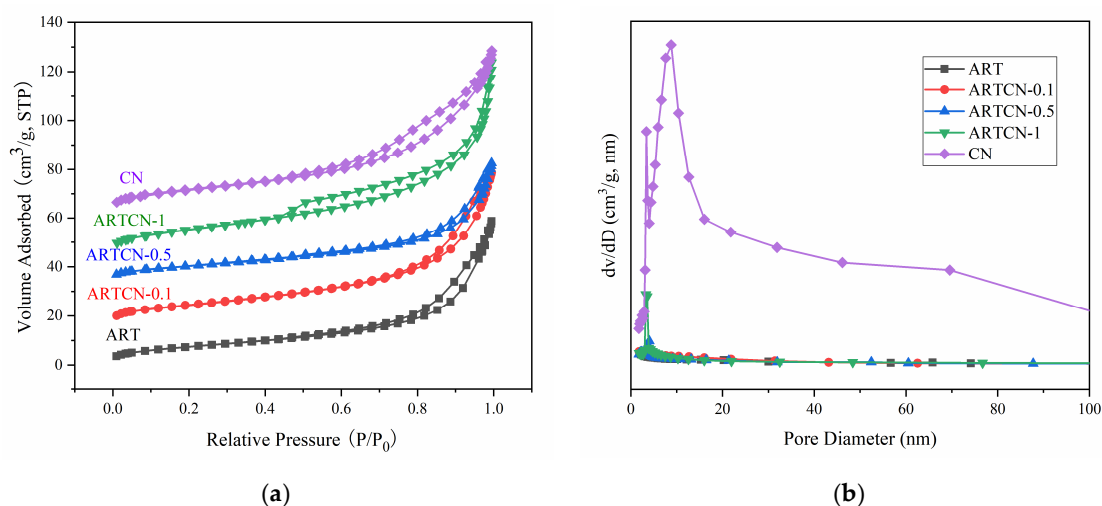


**Figure 4.** N<sub>2</sub> adsorption–desorption curve (a) and pore size distribution (b) of the samples.

**Table 2.** Structural parameters of the samples.

Samples	Specific Surface Area (m <sup>2</sup> /g)	Pore Volume (cm <sup>3</sup> /g)	Pore Diameter (nm)
ART	27.28	0.08	11.28
ARTCN-0.1	33.92	0.09	10.13
ARTCN-0.5	36.16	0.08	9.65
ARTCN-1	38.08	0.12	9.29
CN	42.09	0.11	8.67

### 2.1.5. Optical Performance Analysis

The optical absorption properties of the prepared samples were investigated via the UV–Vis absorption spectra, and the results are shown in Figure 5a. The optical absorption intensity of the ARTCN-X composite material improved by CN widened in the visible light range because the specific ART surface area improved as CN increased, and the agglomeration phenomenon also significantly improved. These results indicated that CN could effectively expand the optical absorption range of ART, thus improving the response and utilization efficiency of visible light. In addition, the band gap width of the prepared material was calculated with the Kubelka-Munk method [34], as shown in Figure 5b. The bandgap widths of ART, ARTCN-0.1, ARTCN-0.5, ARTCN-1, and CN were 3.01, 2.92, 2.86, 2.85, and 2.84 eV, respectively. First, we clearly observed that the band gap width of ART was smaller than the 3.12 eV value reported in the literature, because heterostructures would form between the anatase phase TiO<sub>2</sub> and rutile phase TiO<sub>2</sub>, enhancing the ability of photogenerated carrier separation [35]. Secondly, we found that with the increase in the CN content of the amendment, the band gap width of the composite ARTCN-X became significantly smaller than that of ART and approached that of CN, which was consistent with other studies [36].

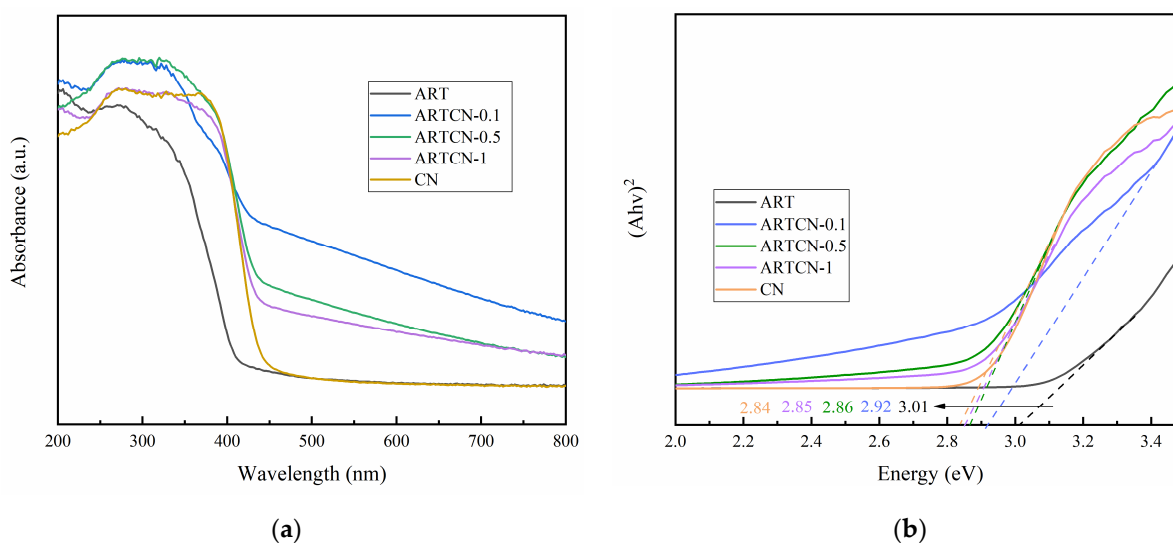


**Figure 5.** Optical properties (a) and the band gap width (b) of the samples.

#### 2.1.6. PL and EPR Analysis

A PL spectrum can be used to study the separation of the photogenerated carriers in semiconductors, where the lower the peak intensity, the lower the recombination rate of the photogenerated carriers and the higher the photocatalytic activity [37]. As shown in Figure 6a, ARTCN-0.5 had the lowest peak intensity, indicating that its photocatalytic activity was the highest, which further indicated that as an amendment, the amount of CN addition did not follow the logic of “the more content the better” but had an appropriate ratio with ART. In addition, we observed that the wide wavelength range of ARTCN-X after CN modification in the interval of 451.8–468.8 nm was attributed to the oxygen vacancy that contained two captured electrons, which both promoted the formation of superoxide radicals ( $\cdot\text{O}_2^-$ ) and hydroxyl radicals ( $\cdot\text{OH}$ ) and was favorable for photocatalytic degradation.

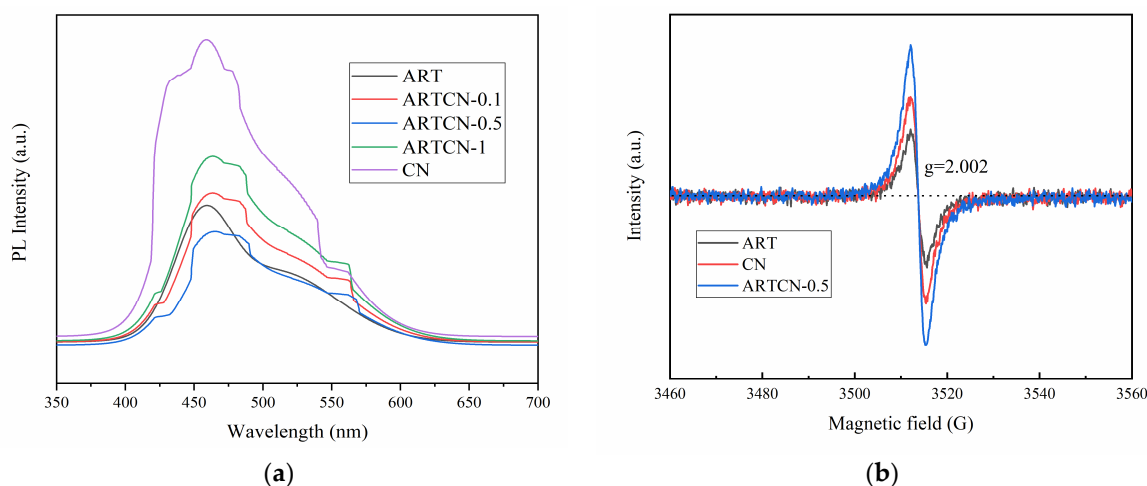


**Figure 6.** PL (a) and (b) EPR of the samples.

Additional EPR spectra that were collected at room temperature provided information regarding the oxygen vacancies (Ov). As shown in Figure 6b, the signal at  $g = 2.002$  corresponded to Ov [38]. We found that all samples had oxygen vacancy signals, and the intensity of ARTCN-0.5 was stronger than that of single ART and CN, which indicated that there was a large amount of Ov that could effectively inhibit the recombination of electrons

and holes and improve the photocatalytic activity, thus confirming the results shown in Figure 6a.

## 2.2. Photocatalytic Performance Test Results

### 2.2.1. Study on the Photocatalytic Degradation of Gaseous Ammonia

The initial concentration of ammonia was  $50 \text{ mg/m}^3$ , and the flow rate of the moist air was  $0.9 \text{ mL/min}$ . Different catalysts were used to study their influence on the degradation of gaseous ammonia, and the results are shown in Figure 7a. This indicated that PET itself was not good at removing gaseous ammonia, and the average degradation rates of gaseous ammonia by ART, ARTCN-0.1, ARTCN-0.5, ARTCN-1, and CN were 52.35%, 61.43%, 88.86%, 63.90%, and 33.51%, respectively. These results indicated that the degradation performance of gaseous ammonia by the ARTCN-X composite catalyst modified by CN was improved, and the effect was most obvious when the amount of CN was  $0.5 \text{ g}$  because ARTCN-0.5 had the strongest photogenerated carrier separation ability.

The initial concentration of ammonia was  $50 \text{ mg/m}^3$ , and the flow rate of moist air was adjusted. ARTCN-0.5 was selected to study its influence on the degradation of gaseous ammonia, and the results are shown in Figure 7b. At  $1.2 \text{ mL/min}$ , the degradation rates of gaseous ammonia by ARTCN-0.5 were 57.93%, 63.98%, 78.26%, 83.38%, 88.86%, 87.10%, and 67.04%. The degradation rates of gaseous ammonia by ARTCN-0.5 first increased and then decreased with the flow rate of moist air. This was because moist air was conducive to the deposition of gaseous ammonia. However, ARTCN-0.5 could oxidize water molecules into hydroxyl radicals ( $\cdot\text{OH}$ ) with strong oxidation in the photocatalytic reaction process, thus improving the efficiency of the photocatalytic reaction. However, ammonia molecules could not tightly bind to the catalyst and flow out of the system before being reacted, resulting in a decrease in its degradation rate.

When the flow rate of moist air was  $0.9 \text{ mL/min}$ , ARTCN-0.5 was selected to study its influence on the degradation of gaseous ammonia, and the results are shown in Figure 7c. When the concentrations of gaseous ammonia were  $30 \text{ mg/m}^3$ ,  $50 \text{ mg/m}^3$ , and  $70 \text{ mg/m}^3$ , the average degradation rates of gaseous ammonia by ARTCN-0.5 were 80.38%, 88.86%, and 73.15%, respectively. The degradation rate decreased if the concentration of gaseous ammonia was too low or too high. This was because ARTCN-0.5 released a limited number of active free radicals after it degraded ammonia when the concentration of gaseous ammonia was too large. Many gaseous ammonia molecules went along with the airflow, and when the concentration of gaseous ammonia was too small, the active radicals could not completely combine with the gaseous ammonia.

The initial concentration of ammonia was  $50 \text{ mg/m}^3$ , and the flow rate of moist air was  $0.9 \text{ mL/min}$ . After the degradation performance of ARTCN-0.5 was tested, PET loaded with ARTCN-0.5 was removed and kept in an oven at  $70 \text{ }^\circ\text{C}$  for 2 h. Then, the test was repeated to explore the reuse performance of ARTCN-0.5; the results are shown in Figure 7d. The average degradation rates for the five reuse cycles were 88.86%, 85.00%, 80.40%, 76.48%, and 70.05%. Given the inevitable catalyst loss in the process of repeated testing, ARTCN-0.5 demonstrated a good overall repeatable degradation performance.

Figure 7e shows the XRD patterns of ARTCN-0.5 before and after repeated use (five times). We found that the crystal shape and structure of ARTCN-0.5 did not significantly change after five repeated uses, indicating that its properties were stable.

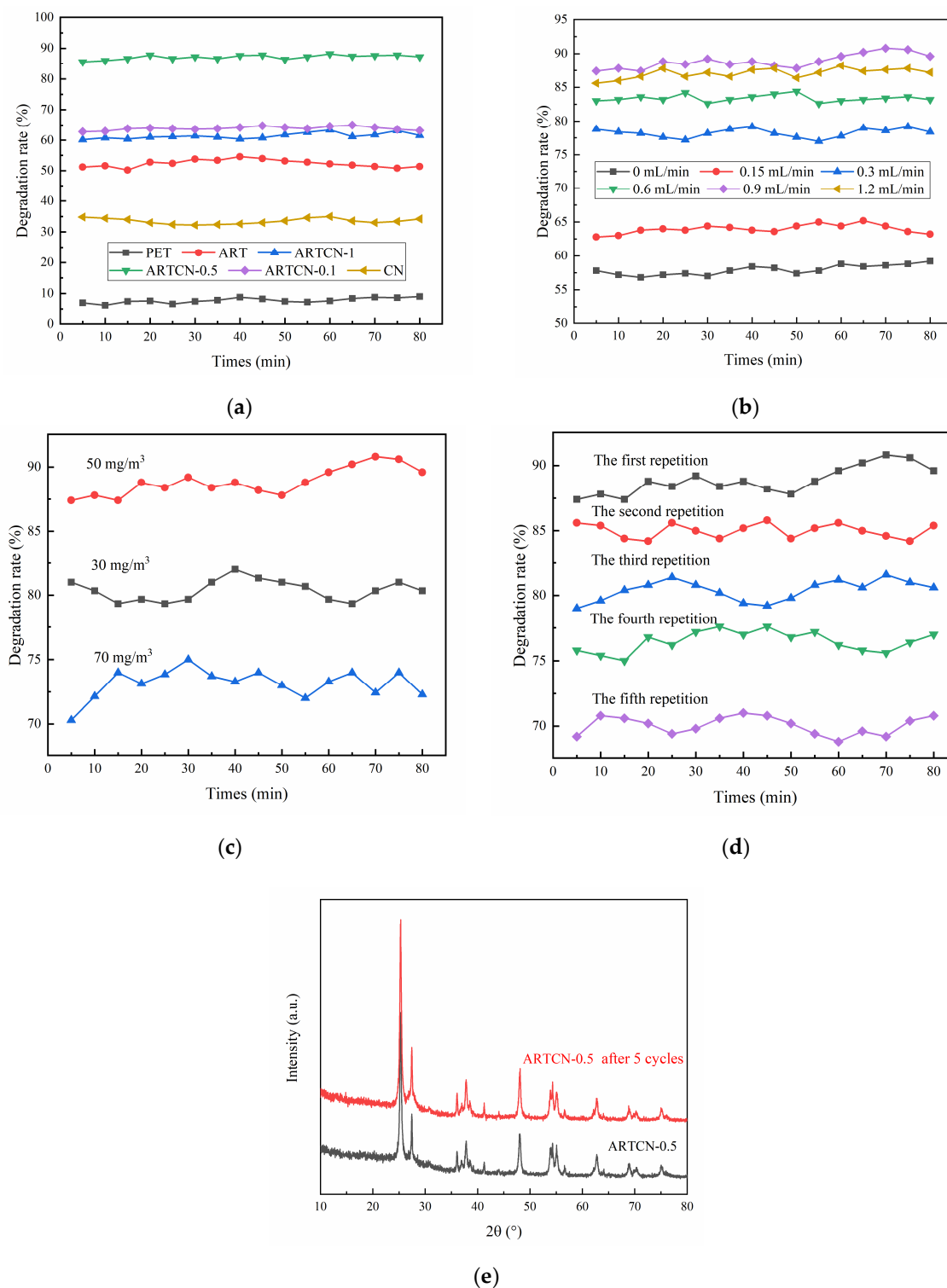


**Figure 7.** Influence of different catalysts on the degradation of gaseous ammonia (a), the effect of different humid air flow rates on the degradation of gaseous ammonia (b), the effects of different ammonia concentrations on the degradation of gaseous ammonia (c), the repeated degradation performance of ARTCN-0.5 (d), and XRD patterns before and after the repeated use (5 times) of ARTCN-0.5 (e).

### 2.2.2. Study on the Photocatalytic Degradation of Liquid Ammonia

When pH > 10, NH<sub>4</sub><sup>+</sup> hydrolyzes in an alkaline solution and then exists in the form of NH<sub>3</sub>·H<sub>2</sub>O [39]. Therefore, we chose to adjust the pH of ammonia nitrogen to 10.1, and

then we tested the concentration of ammonia nitrogen in the solution. We found that it decreased by 3.82% because a small amount of  $\text{NH}_3 \cdot \text{H}_2\text{O}$  escaped in the gaseous form. The degradation results of ammonia nitrogen by different catalysts are shown in Figure 8a, where the catalytic dose was 50 mg and the initial concentration of  $\text{NH}_4^+$  was 100 mg/L. The degradation rates of liquid ammonia by ART, ARTCN-0.1, ARTCN-0.5, ARTCN-1, and CN after 3 h of reaction were 50.54%, 63.18%, 71.60%, 53.55%, and 37.91%, respectively, indicating that the degradation performance of the gaseous ammonia by the ARTCN-X composite catalyst after CN improvement was improved.

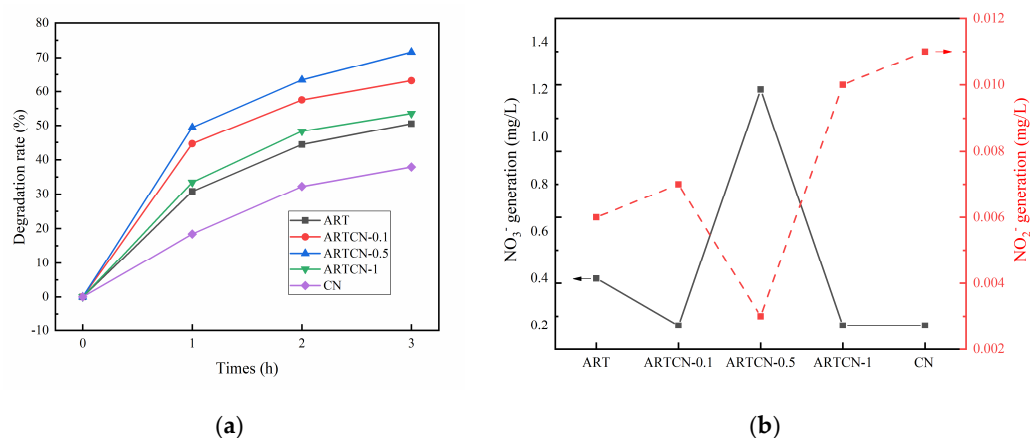


**Figure 8.** Degradation of the liquid ammonia by samples (a);  $\text{NO}_3^-$  and  $\text{NO}_2^-$  production after the reaction (b).

When the initial concentration of ammonia nitrogen was 100 mg/L, 50 mg of ARTCN-0.5 catalyst was added, the pH was 10.1, and the reaction was performed after 3 h. The results are shown in Figure 8b, which shows that the  $\text{NO}_3^-$  and  $\text{NO}_2^-$  concentrations were not greater than 1.4 and 0.012 mg/L, respectively. According to the literature reports, there are three main reaction products of ammonia nitrogen, nitrate, nitrite, and nitrogen, and ammonia nitrogen is mainly oxidized to  $\text{N}_2$  [40].

### 3. Discussion

#### 3.1. Charge Transfer Mechanism Discussion

To understand the reason for the observed improved photocatalytic performance, we proposed a charge separation and transfer mechanism. The conduction band position of a semiconductor could be calculated by the empirical formulas shown in Equations (2) and (3) [41]:

$$E_c = \chi - E_e - E_g/2 \quad (2)$$

$$E_v = E_c + E_g \quad (3)$$

where  $\chi$  is the geometric mean of the absolute electronegativity of each atom in the semiconductor, with  $\text{TiO}_2$  [42] and  $\text{g-C}_3\text{N}_4$  [43]  $\chi$  values of 5.81 eV and 4.82 eV, respectively;  $E_e$  is a constant relative to the standard hydrogen electrode of about 4.5 eV [44];  $E_g$  is the semiconductor band gap width;  $E_v$  is the semiconductor valence band energy; and  $E_c$  is the semiconductor conduction band energy.

According to the analysis presented in Figure 5b, the  $E_g$  values of  $\text{TiO}_2$  and  $\text{g-C}_3\text{N}_4$  were 3.01 and 2.84 eV, respectively. We calculated that the  $E_v$  and  $E_c$  values of ART were 2.815 and  $-0.195$  eV, respectively, the  $E_v$  and  $E_c$  of  $\text{g-C}_3\text{N}_4$  had a value of 1.59, and  $E_c$  was  $-1.25$  V(vs NHE). CN was more negative than ART, and the  $E_v$  of ART was higher than that of CN. The high photocatalytic activity of the heterojunctions between ARTCN could be explained by the following mechanism.

Two possibilities existed for the photocatalytic mechanism of the composite catalyst: (1) conventional type II heterojunctions and (2) Z-type heterojunctions [45]. Under sim-

ulated solar irradiation, ART and CN were excited and generated electron-hole pairs. If the type II heterojunction mechanism was followed, the photogenerated electrons in the conduction band of CN would be transferred to the conduction band of ART and the photogenerated holes in the valence band of ART would be transferred to the valence band of CN [46], as shown in Figure 9a. However, the hole in the valence band of CN could not generate ·OH by reacting with H<sub>2</sub>O. This was because the valence band potential of CN (1.59 eV) was lower than the standard oxidation potential E (H<sub>2</sub>O/·OH) (2.38 eV) [47], resulting in a decrease in ·OH content, which was inconsistent with the results shown in Figure 9b. If the charge transfer mechanism of the Z-type heterostructure was followed, the photogenerated electrons in the ART conduction band would transfer to the valence band of CN and combine with the photogenerated holes in the CN valence band. This would result in a reduction in electrons in ARTCN and the accumulation of electrons in the CN conduction band and holes in the ART valence band, which was why the content of ·O<sub>2</sub><sup>-</sup> produced by CN shown in Figure 10a was higher than that of ARTCN. The holes that accumulated in the valence band of ART had strong oxidability and could directly degrade ammonia molecules. However, the E<sub>c</sub> (-1.10 V) of CN was more negative than E<sub>0</sub> (O<sub>2</sub>/·O<sub>2</sub><sup>-</sup>), and the electrons that accumulated in the conduction band of CN could react with O<sub>2</sub> to generate ·O<sub>2</sub><sup>-</sup>. This z-type heterostructure was more consistent with the characterization results of ESR (Figure 10).

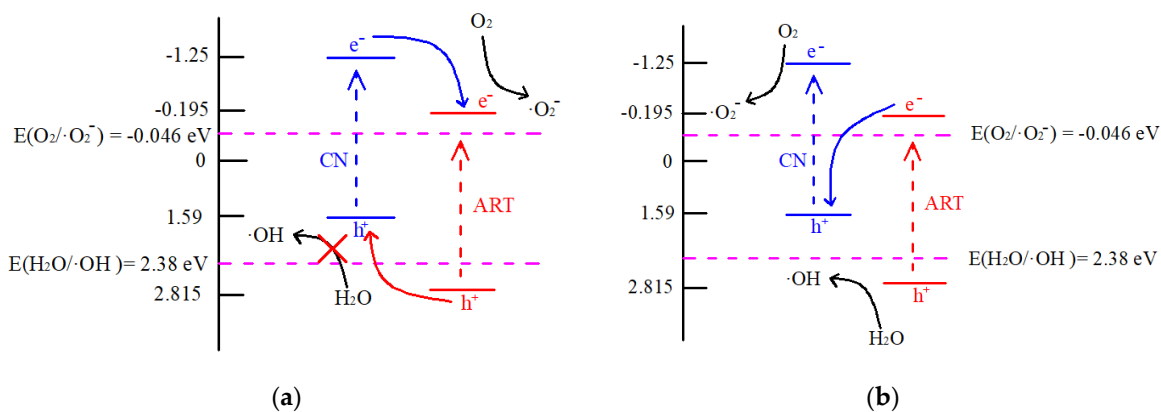


Figure 9. Charge transfer mechanism of the photocatalytic degradation conventional type II heterojunction (a) and Z-type heterostructure (b).

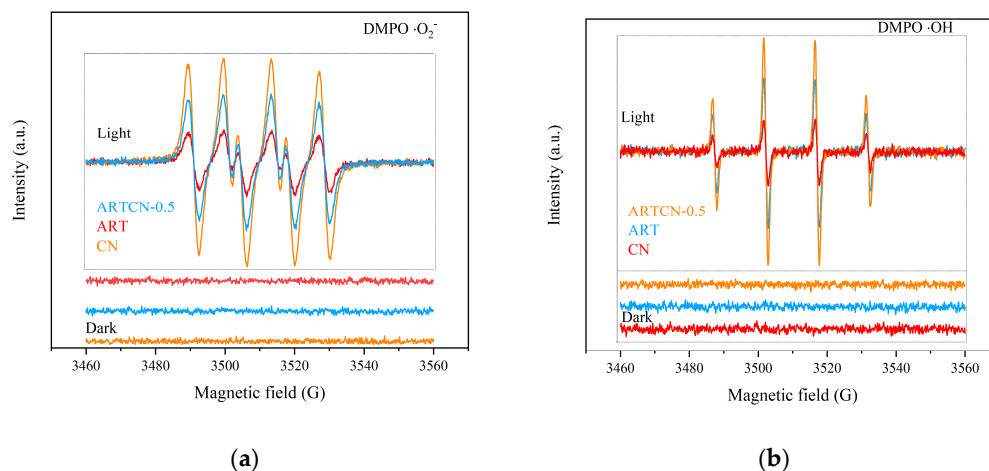
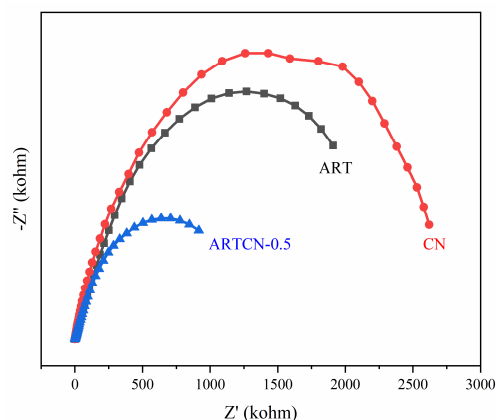


Figure 10. ESR profiles of DMPO ·O<sub>2</sub><sup>-</sup> (a) and DMPO ·OH (b) of the samples.

To further verify the accuracy of the above results, the test results of EIS are presented in Figure 11, which shows the impedance diagrams of ART, CN, and ARTCN. The electron

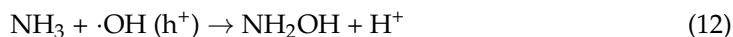
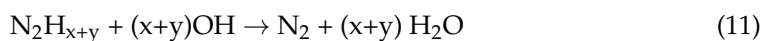
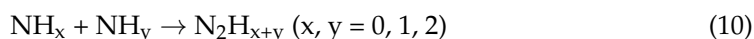
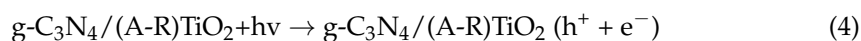
transfer resistance in the sample was equivalent to the semicircle diameter on the EIS diagram, where the smaller the arc radius, the lower the charge transfer resistance of the composite sample [48]. Hence, due to the formation of the Z-type heterostructure, the charge-transfer resistance of ARTCN-0.5 was lower than ART and CN, which significantly improved the efficiency of photogenerated electron-hole migration and separation, which was consistent with the work of Y.Y. Wang [49].



**Figure 11.** EIS spectra of the samples.

### 3.2. Photocatalytic Degradation Mechanism Discussion

ESR was used to detect the types of free radicals in the catalysts under light, and then we explored their degradation mechanism of ammonia. As shown in Figure 10a,b, ART, CN, and ARTCN-0.5 did not produce free radicals in the absence of light, and superoxide free radicals ( $\cdot\text{O}_2^-$ ) and hydroxyl free radicals ( $\cdot\text{OH}$ ) were detected after light exposure.  $\cdot\text{O}_2^-$  and  $\cdot\text{OH}$  played decisive roles in the entire reaction [50]. The degradation mechanism was as follows. After gaseous ammonia combined with moist air,  $\text{NH}_4^+$  was present as  $\text{NH}_3\cdot\text{H}_2\text{O}$  under alkaline conditions. First, when the catalyst was illuminated, electrons and holes were generated [51]. The holes oxidized the water molecules on the surface of the catalyst, forming  $\cdot\text{OH}$ , while the electrons and dissolved oxygen underwent a series of reactions to form  $\cdot\text{O}_2^-$ , following Equations (4)–(6) [52].  $\cdot\text{OH}$  and  $\cdot\text{O}_2^-$  were the main active components in the photocatalytic reaction process, and they could rapidly oxidize the  $\text{NH}_4^+/\text{NH}_3/\text{NH}_3\cdot\text{H}_2\text{O}$  adsorbed on the surface of the catalyst [53]. Equations (9)–(13) show that ammonia was directly and completely oxidized to  $\text{N}_2$  [54], and the  $\text{NO}_3^-$  and  $\text{NO}_2^-$  contents were very low after the reaction. Equations (12)–(16) show that ammonia was not completely oxidized to  $\text{NO}_3^-$  and  $\text{NO}_2^-$ , which was consistent with the research of Sun et al. [55].





## 4. Materials and Methods

### 4.1. Materials

Ammonium chloride (AR, Chengdu Colon Chemicals Co., Ltd. Chengdu, Sichuan province, China), butyl titanate (AR, Chengdu Colon Chemicals Co., Ltd. Chengdu, Sichuan province, China), absolute ethanol (AR, Chongqing Chuandong Chemical Co., Ltd. Nanan district, Chongqing, China), urea (AR, Sinopharm Chemical Reagent Co., Ltd. Huangpu district, Shanghai, China), and NaOH (AR, Chongqing Chuandong Chemical Co., Ltd. Nanan district, Chongqing, China) were used in this study.

### 4.2. Preparation of Catalysts

We added 30 mL of absolute ethanol to 35 mL of butyl titanate, which was denoted as solution A. Then, we added 30 mL of absolute ethanol to 100 mL of distilled water, which was denoted as solution B. Solution A was dropwise added to solution B at 4 drops per second, and then it was mixed and stirred at a low speed for 2 h to obtain the  $\text{TiO}_2$  gel, which was aged at room temperature. The aged  $\text{TiO}_2$  gel was transferred to a stainless steel reaction kettle with a polytetrafluoron liner and maintained at 100 °C for 2 h. After cooling, it was centrifuged and settled, washed with deionized water and ethanol 3 times, and dried in a 100 °C air-drying oven. Then, the  $\text{TiO}_2$  catalyst powder was obtained after grinding. The  $\text{TiO}_2$  powder was maintained at 600 °C for 2 h at a heating rate of 10 °C/min, and then it was cooled to room temperature and ground to obtain ART.

Subsequently, 10 g of urea and 50 mL of water were added to the crucible and evenly stirred. The crucible was placed in a muffle furnace and maintained at 500 °C for 2 h at a heating rate of 10 °C/min. After the heating program was finished and the muffle furnace naturally cooled, the obtained bulk particles were ground to obtain CN.

We mixed 0.1 g of CN, 0.5 g of CN, 1 g of CN, and 1 g of ART; added 5 mL of absolute ethanol; stirred evenly; and then separated and dispersed the mixture using a cell fragmentation apparatus (Ningbo, Zhejiang Province, China. Xinzhi Biotechnology Co., Ltd., SCIENTZ-IIID, 65 Hibiscus Road, Ningbo National High-tech Zone). Maintaining the temperature at 300 °C for 2 h at a heating rate of 10 °C/min, ARTCN-X was obtained and is denoted as ARTCN-0.1, ARTCN-0.5, and ARTCN-1.

### 4.3. Fixation of Photocatalytic Materials

We washed the polyester fiber cotton (PET) with 1 mol/L of NaOH to remove the surface impurities, and then we dried and set it aside. Subsequently, 100 mg of catalyst was dissolved in water, the treated PET was added and shaken in a shaker for 30 min, and the water on the surface and the excess catalyst were drained before the catalyst was dried at 70 °C for later use. The PET scanning electron microscope results before and after catalyst loading are shown in Figure 12. We clearly observed that the photocatalytic materials were evenly loaded on PET.

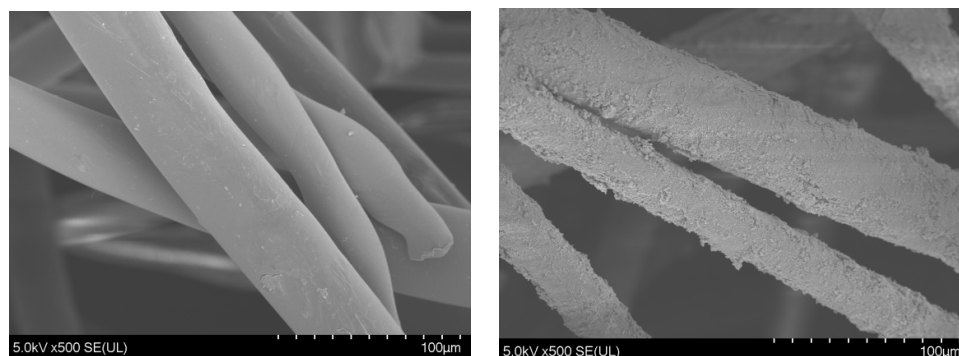


**Figure 12.** SEM of the PET scan before and after catalyst support.

#### 4.4. Catalyst Characterization

A D8 Advance model X-ray diffractometer (XRD, Bruker, Germany) was used to analyze the crystal characteristics of the catalyst. The operating parameters were a Cu X-ray tube target and a scanning range of 10–80°. An HR800 laser confocal Raman spectrometer (Raman, Horiba Jobin Yvon, France) was used to detect the sample structures, where the excitation wavelength was 633 nm. A TriStar II 3020 series automatic specific surface analyzer (BET, GA, USA) was used to determine the specific surface area and porosity of the catalyst. The catalyst was pretreated under vacuum degassing at 200 °C for 5 h, and high-purity nitrogen was used as the adsorbent at 77 K. Then, a UV–Vis diffuse reflectance (UV–Vis DRS, Hitachi, Japan) instrument (model U-3010) was used to test the optical properties of the catalyst in the range of 200–800 nm. An F-2700 fluorescence spectrophotometer (PL, Japan, Hitachi) was used to measure the electron hole recombination, with an operating voltage of 250 V, a wavelength of 5 nm, and an excitation wavelength of 300 nm. The surface morphology and elemental distribution of the samples were analyzed by scanning electron microscopy (SEM, Sigma500, Germany) and an energy dispersive spectrometer (EDS, Bruker, Germany). Transmission electron microscopy (TEM, FEI TalOS F200S, USA) was used to analyze the lattice spacings of the samples. Fluorescence spectrophotometry (PL, HORIBA, Osaka, Japan) was used to test the photogenerated carrier separation of the catalyst with a hydrogen light source with a pulse width of 1.0 to 1.6 ns, which was used to test the fluorescence lifetime of the sample. Electron paramagnetic resonance (EPR, Bruker, Germany) was performed at room temperature using an A300 spectrometer, and 5,5-dimethyl-1-pyrroline N-oxide (DMPO) was used as the spin capture agent for ESR analysis. A CHI-660C electrochemical workstation was used for transient photocurrent measurements. A Na<sub>2</sub>SO<sub>4</sub> aqueous solution (1 M) was used as the electrolyte solution, and electrochemical impedance spectroscopy (EIS, Chenhua, China) measurements were performed under visible light irradiation with frequencies ranging from  $4 \times 10^6$  to  $1 \times 10^{-2}$  Hz.

#### 4.5. Photocatalytic Activity Tests

##### 4.5.1. Degradation of Gaseous Ammonia

Figure 13 shows the device diagram for the photocatalytic degradation of gaseous ammonia. The light source consisted of a 300 W xenon lamp ( $30.2 \text{ mW/cm}^2$ ), which was installed in a quartz water pipe with a condensation cycle to absorb the heat generated by illumination. Just below the xenon lamp was a photocatalytic quartz reaction tube, and PET loaded with the photocatalytic materials was placed in the tube. After exiting the cylinder, ammonia entered the reaction tube through a flowmeter. The different concentrations of standard ammonia (mixed with nitrogen) were  $30 \text{ mg/m}^3$ ,  $50 \text{ mg/m}^3$ , and  $70 \text{ mg/m}^3$ , with a flow rate of 100 mL/min, and the stability test results of the different concentrations of ammonia are shown in Figure 14. Air entered the photocatalytic reaction tube through the water, needle valve, and flowmeter in turn (moist air was the only source of oxygen). Ammonia was mixed with air at a certain humidity to simulate gaseous ammonia. After

connecting each pipeline, the standard gas was ventilated to determine whether there was air leakage. The system was run for 10 min until it was stable, and the degradation efficiency of the gaseous ammonia in the entire process was  $\eta_1$  (Equation (17)):

$$\eta_1 = (C_{01} - C_1) \times 100\%/C_{01} \tag{17}$$

where  $C_{01}$  is the standard concentration of gaseous ammonia ( $\text{mg}/\text{m}^3$ ) and  $C_1$  is the concentration of gaseous ammonia in the reaction process ( $\text{mg}/\text{m}^3$ ).

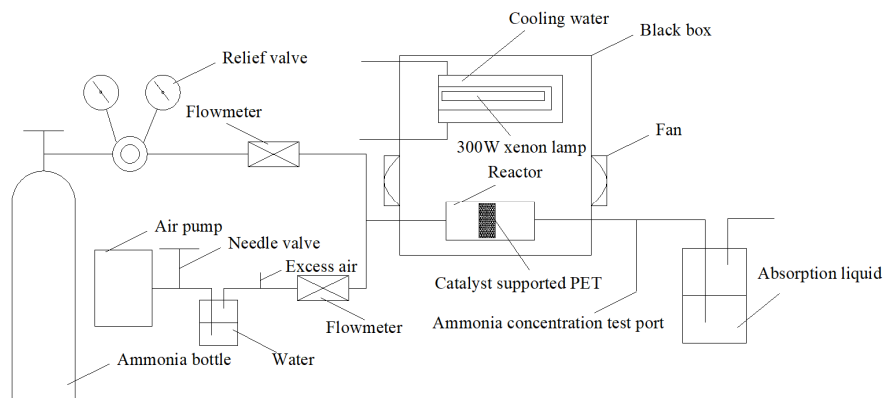


Figure 13. Device diagram of the photocatalytic degradation of gaseous ammonia.

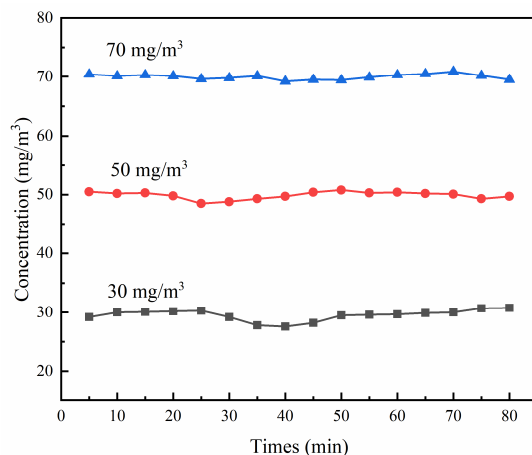


Figure 14. System stability test.

#### 4.5.2. Degradation of Liquid Ammonia

The photoreactor consisted of a 200 mL double-layer quartz beaker, for which the outer layer was permeated with cooling water to ensure a constant reaction temperature and the inner layer consisted of 100 mg/L of an ammonia nitrogen solution. The pH was adjusted to 10.1 by sodium hydroxide. The 300 W xenon lamp ( $30.2 \text{ mW}/\text{m}^2$ ) was used as the light source to simulate sunlight while ensuring that the distance between the xenon lamp and the liquid level was 15 cm. Then, 50 mg (0.5 g/L) of catalyst was added to the solution and stirred at medium speed at room temperature; 2 mL of the sample from the reaction solution was extracted every 60 min and centrifuged for 10 min with a 10,000 r/min high-speed centrifuge, and the supernatant was obtained to determine the concentration of ammonia nitrogen and calculate its degradation rate  $\eta_2$  (Equation (18)). The nitrate and nitrite concentrations were determined after the reaction:

$$\eta_2 = (C_{02} - C_2) \times 100\%/C_{02} \tag{18}$$

where  $C_{02}$  is the initial concentration of ammonia nitrogen and  $C_2$  is the concentration of ammonia nitrogen in the reaction process (mg/L).

## 5. Conclusions

A g-C<sub>3</sub>N<sub>4</sub>/(A-R)TiO<sub>2</sub> composite catalyst (ARTCN) was prepared by using g-C<sub>3</sub>N<sub>4</sub> (CN) as the amendment, and the amount of CN had a great influence on the performance of ARTCN. When the amount of CN was 0.5 g, ARTCN-0.5 had a better dispersion, a smaller band gap width, a larger specific surface area, a stronger light absorption capacity, and a stronger photogenerated carrier separation ability than ART.

The air wetness and initial concentration of the ammonia had a great influence on the degradation of the gaseous ammonia. When the initial concentration of ammonia was 50 mg/m<sup>3</sup> and the flow rate of the moist air was 0.9 mL/min, the degradation rate of gaseous ammonia by ARTCN-0.5 reached 88.86%, and it had good repeatability. When the catalytic dose was 50 mg and the initial concentration of NH<sub>4</sub><sup>+</sup> was 100 mg/L, the degradation rate of the liquid ammonia by ARTCN-0.5 was 71.60% at 3 h, and small amounts of NO<sub>3</sub><sup>-</sup> and NO<sub>2</sub><sup>-</sup> were generated. Subsequently, ·OH and ·O<sub>2</sub><sup>-</sup> were the main active components in the photocatalytic reaction process.

The photogenerated electrons in the conduction band of ART transferred to the valence band of CN and combined with the photogenerated holes in the valence band of CN, forming a Z-type heterostructure that significantly improved the efficiency of the photogenerated electron-hole migration and separation, thus increasing the reaction rate.

**Author Contributions:** Conceptualization: J.Z. and S.P.; data curation: Y.J.; investigation and methodology: H.W.; project administration: Z.L.; resources, J.Z. and Z.L.; supervision, J.Z. and D.L.; writing—original draft: J.Z. and S.P.; writing—review and editing: D.L. and J.Z. All authors have read and agreed to the published version of the manuscript.

**Funding:** Financial support was provided by the Chongqing scientific research institution performance Incentive and guidance special project (cstc2020xj20006), National Center of Technology Innovation for Pigs, Chongqing 402460, China. The Modern agroindustry technology research system (CARS-35, 21203).

**Institutional Review Board Statement:** Not applicable.

**Informed Consent Statement:** Not applicable.

**Data Availability Statement:** Not applicable.

**Acknowledgments:** We thank the editors of MDPI for their patience during the processing of this manuscript.

**Conflicts of Interest:** There are no conflict of interest in the manuscript submission, and it has been approved by all authors for publication. All authors listed have approved the enclosed manuscript.

## References

1. Clarisse, L.; Clerbaux, C.; Dentener, F.J.; Hurtmans, D.; Coheur, P.F. Global ammonia distribution derived from infrared satellite observations. *Nat. Geosci.* **2009**, *2*, 479. [[CrossRef](#)]
2. Van Damme, M.; Clarisse, L.; Whitburn, S.; Hadji-Lazaro, J.; Hurtmans, D.; Clerbaux, C.; Coheur, P.F. Industrial and agricultural ammonia point sources exposed. *Nature* **2018**, *564*, 99. [[CrossRef](#)] [[PubMed](#)]
3. Schaubberger, G.; Piringer, M.; Mikovits, C.; Zollitsch, W.; Hörtenhuber, S.; Baumgartner, J.; Niebuhr, K.; Anders, I.; Andre, K.; Hennig, P.I.; et al. Impact of global warming on the odour and ammonia emissions of livestock buildings used for fattening pigs. *Biosyst. Eng.* **2018**, *175*, 106. [[CrossRef](#)]
4. Derwent, R.; Witham, C.; Redington, A.; Jenkin, M.; Stedman, J.; Yardley, R.; Hayman, G. Particulate matter at a rural location in southern England during 2006: Model sensitivities to precursor emissions. *Atmos. Environ.* **2013**, *69*, 211. [[CrossRef](#)]
5. Bessagnet, B.; Beauchamp, M.; Guerreiro, C.D.B.B.; de Leeuw, F.; Tsyro, S.; Colette, A.; Meleux, F.; Rouil, L.; Ruysenaars, P.; Sauter, F.; et al. Can further mitigation of ammonia emissions reduce exceedances of particulate matter air quality standards? *Environ. Sci. Policy* **2014**, *44*, 149. [[CrossRef](#)]
6. Pearson, J.; Stewart, G.R. The deposition of atmospheric ammonia and its effects on plants. *New Phytol.* **1993**, *125*, 283. [[CrossRef](#)]
7. Pu, S.; Long, D.; Liu, Z.; Yang, F.; Zhu, J. Preparation of RGO-P25 Nanocomposites for the Photocatalytic Degradation of Ammonia in Livestock Farms. *Catalysts* **2018**, *8*, 189. [[CrossRef](#)]

8. Zhu, J.; Jian, Y.; Long, D.; Wang, H.; Zeng, Y.; Li, J.; Xiao, R.; Pu, S. Degradation of ammonia gas by  $\text{Cu}_2\text{O}/\{001\}\text{TiO}_2$  and its mechanistic analysis. *RSC Adv.* **2021**, *11*, 3695. [[CrossRef](#)]
9. Enesca, A.; Andronic, L.; Duta, A. Optimization of Opto-Electrical and Photocatalytic Properties of  $\text{SnO}_2$  Thin Films Using  $\text{Zn}^{2+}$  and  $\text{W}^{6+}$  Dopant Ions. *Catal. Lett.* **2012**, *142*, 224. [[CrossRef](#)]
10. Hu, X.; Guo, R.T.; Chen, X.; Bi, Z.X.; Wang, J.; Pan, W.-G. Bismuth-based Z-scheme structure for photocatalytic  $\text{CO}_2$  reduction: A review. *J. Environ. Chem. Eng.* **2022**, *10*, 108582. [[CrossRef](#)]
11. Liu, X.; Xu, J.; Jiang, Y.; Du, Y.; Zhang, J.; Lin, K. In-situ construction of  $\text{CdS@ZIS}$  Z-scheme heterojunction with core-shell structure: Defect engineering, enhance photocatalytic hydrogen evolution and inhibit photo-corrosion. *Int. J. Hydrog. Energy* **2022**, *47*, 35241. [[CrossRef](#)]
12. Kolinko, P.A.; Kozlov, D.V. Products distribution during the gas phase photocatalytic oxidation of ammonia over the various titania based photocatalysts. *Appl. Catal. B Environ.* **2009**, *90*, 126. [[CrossRef](#)]
13. Wu, H.; Ma, J.; Li, Y.; Zhang, C.; He, H. Photocatalytic oxidation of gaseous ammonia over fluorinated  $\text{TiO}_2$  with exposed (001) facets. *Appl. Catal. B Environ.* **2014**, *152*, 82. [[CrossRef](#)]
14. Wang, J.Y.; Liu, B.S.; Nakata, K. Effects of crystallinity, {001}/{101} ratio, and Au decoration on the photocatalytic activity of anatase  $\text{TiO}_2$  crystals. *Chin. J. Catal.* **2019**, *40*, 403. [[CrossRef](#)]
15. Hosono, E.; Fujihara, S.; Kakiuchi, A.K.; Imai, H. Growth of submicrometer-scale rectangular parallelepiped rutile  $\text{TiO}_2$  films in aqueous  $\text{TiCl}_3$  solutions under hydrothermal conditions. *J. Am. Chem. Soc.* **2004**, *126*, 7790. [[CrossRef](#)] [[PubMed](#)]
16. Shen, S.; Wang, X.; Chen, T.; Feng, Z.; Li, C. Transfer of photoinduced electrons in anatase-rutile  $\text{TiO}_2$  determined by time-resolved midinfrared spectroscopy. *J. Phys. Chem. C* **2014**, *118*, 12661. [[CrossRef](#)]
17. Das, B.; Nair, R.G.; Rajbongshi, B.; Samdarshi, S. Investigation of the Photoactivity of Pristine and Mixed Phase N-doped Titania under Visible and Solar Irradiation. *Mater. Charact.* **2013**, *83*, 145–151. [[CrossRef](#)]
18. Xiong, J.Y.; Zhang, M.M.; Cheng, G. Facile polyol triggered anatase-rutile heterophase  $\text{TiO}_2$ -x nanoparticles for enhancing photocatalytic  $\text{CO}_2$  reduction. *J. Colloid Interface Sci.* **2020**, *579*, 872. [[CrossRef](#)]
19. Rani, S.; Garg, A.; Singh, N. Highly efficient photo-degradation of cetirizine antihistamine with  $\text{TiO}_2$ - $\text{SiO}_2$  photocatalyst under ultraviolet irradiation. *Int. J. Chem. React. Eng.* **2022**, *20*, 183. [[CrossRef](#)]
20. Guarino, M.; Costa, A.; Porro, M. Photocatalytic  $\text{TiO}_2$  coating to reduce ammonia and greenhouse gases concentration and emission from animal husbandries. *Bioresour. Technol.* **2008**, *99*, 2650. [[CrossRef](#)]
21. Pu, S.; Wang, H.; Zhu, J.; Li, L.; Long, D.; Jian, Y.; Zeng, Y. Heterostructure  $\text{Cu}_2\text{O}/(001)\text{TiO}_2$  Effected on Photocatalytic Degradation of Ammonia of Livestock Houses. *Catalysts* **2019**, *9*, 267. [[CrossRef](#)]
22. Liu, C.H.; Dai, H.L.; Tan, C.Q.; Pan, Q.Y.; Hu, F.P.; Peng, X.M. Photo-Fenton degradation of tetracycline over Z-scheme  $\text{Fe-g-C}_3\text{N}_4/\text{Bi}_2\text{WO}_6$  heterojunctions: Mechanism insight, degradation pathways and DFT calculation. *Appl. Catal. B Environ.* **2022**, *310*, 121326. [[CrossRef](#)]
23. Luan, S.; Qu, D.; An, L.; Jiang, W.; Gao, X.; Hua, S.; Miao, X.; Wen, Y.; Sun, Z. Enhancing photocatalytic performance by constructing ultrafine  $\text{TiO}_2$  nanorods/g- $\text{C}_3\text{N}_4$  nanosheets heterojunction for water treatment. *Sci. Bull.* **2018**, *63*, 683. [[CrossRef](#)]
24. Al-Hajji, L.; Ismail, A.A.; Atitar, M.F.; Abdelfattah, I.; El-Toni, A.M. Construction of mesoporous g- $\text{C}_3\text{N}_4/\text{TiO}_2$  nanocrystals with enhanced photonic efficiency. *Ceram. Int.* **2019**, *45*, 1265. [[CrossRef](#)]
25. Zhao, S.; Chen, S.; Yu, H.; Quan, X. g- $\text{C}_3\text{N}_4/\text{TiO}_2$  hybrid photocatalyst with wide absorption wavelength range and effective photogenerated charge separation. *Sep. Purif. Technol.* **2012**, *99*, 50. [[CrossRef](#)]
26. Sun, M.; Shen, S.; Wu, Z.; Tang, Z.; Shen, J.; Yang, J. Rice spike-like g- $\text{C}_3\text{N}_4/\text{TiO}_2$  heterojunctions with tight-binding interface by using sodium titanate ultralong nanotube as precursor and template. *Ceram. Int.* **2018**, *44*, 8125. [[CrossRef](#)]
27. Li, Y.; Zhang, M.Q.; Liu, Y.F.; Sun, Y.X.; Zhao, Q.H.; Chen, T.L.; Chen, Y.F.; Wang, S.F. In Situ Construction of Bronze/Anatase  $\text{TiO}_2$  Homogeneous Heterojunctions and Their Photocatalytic Performances. *Nanomaterials* **2022**, *12*, 1122. [[CrossRef](#)]
28. Chouhan, L.; Srivastava, S.K. Observation of room temperature d0 ferromagnetism, band-gap widening, zero dielectric loss and conductivity enhancement in Mg doped  $\text{TiO}_2$  (rutile + anatase) compounds for spintronics applications. *J. Solid State Chem.* **2022**, *307*, 122828. [[CrossRef](#)]
29. Mirhosseini, H.; Mostafavi, A.; Shamspur, T.; Sargazi, G. Fabrication of an efficient ternary  $\text{TiO}_2/\text{Bi}_2\text{WO}_6$  nanocomposite supported on g- $\text{C}_3\text{N}_4$  with enhanced visible light photocatalytic activity: Modeling and systematic optimization procedure. *Arab. J. Chem.* **2022**, *15*, 103729. [[CrossRef](#)]
30. Guan, Y.; Wu, J.; Wang, L.; Shi, C.; Lv, K.; Lv, Y. Application of g- $\text{C}_3\text{N}_4/\text{CNTs}$  nanocomposites in energy and environment. *Energy Rep.* **2022**, *8*, 1190. [[CrossRef](#)]
31. Hou, C.T.; Hu, B.; Zhu, J.M. Photocatalytic Degradation of Methylene Blue over  $\text{TiO}_2$  Pretreated with Varying Concentrations of  $\text{NaOH}$ . *Catalysts* **2018**, *8*, 575. [[CrossRef](#)]
32. Chen, Y.; Mao, G.; Tang, Y.; Wu, H.; Wang, G.; Zhang, L.; Liu, Q. Synthesis of core-shell nanostructured  $\text{Cr}_2\text{O}_3/\text{C@TiO}_2$  for photocatalytic hydrogen production. *Chin. J. Catal.* **2021**, *42*, 225. [[CrossRef](#)]
33. Wang, J.; Wang, G.; Jiang, J.; Wan, Z.; Su, Y.; Tang, H. Insight into charge carrier separation and solar light utilization: rGO decorated 3D  $\text{ZnO}$  hollow microspheres for enhanced photocatalytic hydrogen evolution. *J. Colloid Interface Sci.* **2020**, *564*, 322. [[CrossRef](#)] [[PubMed](#)]

34. Li, L.; Ouyang, W.; Zheng, Z.; Ye, K.; Guo, Y.; Qin, Y.; Wu, Z.; Lin, Z.; Wang, T.; Zhang, S. Synergetic photocatalytic and thermocatalytic reforming of methanol for hydrogen production based on Pt@TiO<sub>2</sub> catalyst. *Chin. J. Catal.* **2022**, *43*, 1258. [[CrossRef](#)]
35. Chen, M.; Chen, J.; Chen, C.; Zhang, C.; He, H. Distinct photocatalytic charges separation pathway on CuOx modified rutile and anatase TiO<sub>2</sub> under visible light. *Appl. Catal. B Environ.* **2022**, *300*, 120735. [[CrossRef](#)]
36. Wei, T.; Xu, J.; Kan, C.; Zhang, L.; Zhu, X. Au tailored on g-C<sub>3</sub>N<sub>4</sub>/TiO<sub>2</sub> heterostructure for enhanced photocatalytic performance. *J. Alloy. Compd.* **2022**, *894*, 162338. [[CrossRef](#)]
37. Kubiak, A.; Grzegórska, A.; Zembrzuska, J.; Zielińska, J.A.; Siwińska, C.K.; Janczarek, M.; Krawczyk, P.; Jesionowski, T. Design and Microwave-Assisted Synthesis of TiO<sub>2</sub> Lanthanides Systems and Evaluation of Photocatalytic Activity under UV-LED Light Irradiation. *Catalysts* **2021**, *12*, 8. [[CrossRef](#)]
38. Jian, Y.; Liu, H.; Zhu, J.; Zeng, Y.; Liu, Z.; Hou, C.; Pu, S. Transformation of novel TiOF<sub>2</sub> nanoparticles to cluster TiO<sub>2</sub>-{001/101} and its degradation of tetracycline hydrochloride under simulated sunlight. *RSC Adv.* **2020**, *10*, 42860. [[CrossRef](#)]
39. Zhu, J.; Liu, Z.; Yang, F.; Long, D.; Jian, Y.; Pu, S. The Preparation of {001}TiO<sub>2</sub>/TiOF<sub>2</sub> via a One-Step Hydrothermal Method and its Degradation Mechanism of Ammonia Nitrogen. *Materials* **2022**, *15*, 6465. [[CrossRef](#)]
40. Yao, F.; Fu, W.; Ge, X.; Wang, L.; Wang, J.; Zhong, W. Preparation and characterization of a copper phosphotungstate/titanium dioxide (Cu-H<sub>3</sub>PW<sub>12</sub>O<sub>40</sub>/TiO<sub>2</sub>) composite and the photocatalytic oxidation of high concentration ammonia nitrogen. *Sci. Total Environ.* **2020**, *727*, 138425. [[CrossRef](#)]
41. Zhang, H.; Zhang, G.; Zhang, H.; Tang, Q.; Xiao, Y.; Wang, Y.; Cao, J. Facile synthesis hierarchical porous structure anatase-rutile TiO<sub>2</sub>/g-C<sub>3</sub>N<sub>4</sub> composite for efficient photodegradation tetracycline hydrochloride. *Appl. Surf. Sci.* **2021**, *567*, 150833. [[CrossRef](#)]
42. Hao, R.; Wang, G.; Tang, H.; Sun, L.; Xu, C.; Han, D. Template-free preparation of macro/mesoporous g-C<sub>3</sub>N<sub>4</sub>/TiO<sub>2</sub> heterojunction photocatalysts with enhanced visible light photocatalytic activity. *Appl. Catal. B Environ.* **2016**, *187*, 47. [[CrossRef](#)]
43. Zhang, B.; Hu, X.; Liu, E.; Fan, J. Novel S-scheme 2D/2D BiOBr/g-C<sub>3</sub>N<sub>4</sub> heterojunctions with enhanced photocatalytic activity. *Chin. J. Catal.* **2021**, *42*, 1519. [[CrossRef](#)]
44. Hong, Y.; Jiang, Y.; Li, C.; Fan, W.; Yan, X.; Yan, M.; Shi, W. In-situ synthesis of direct solid-state Z-scheme V<sub>2</sub>O<sub>5</sub>/g-C<sub>3</sub>N<sub>4</sub> heterojunctions with enhanced visible light efficiency in photocatalytic degradation of pollutants. *Appl. Catal. B Environ.* **2016**, *180*, 663. [[CrossRef](#)]
45. Wang, S.; Zhao, T.; Tian, Y.; Yan, L.; Su, Z. Mechanistic insight into photocatalytic CO<sub>2</sub> reduction by a Z-scheme g-C<sub>3</sub>N<sub>4</sub>/TiO<sub>2</sub> heterostructure. *New J. Chem.* **2021**, *45*, 11474. [[CrossRef](#)]
46. Yang, D.; Zhao, X.; Chen, Y.; Wang, W.; Zhou, Z.; Zhao, Z.; Jiang, Z. Synthesis of g-C<sub>3</sub>N<sub>4</sub> Nanosheet/TiO<sub>2</sub> Heterojunctions Inspired by Bioadhesion and Biomineralization Mechanism. *Ind. Eng. Chem. Res.* **2019**, *58*, 5516–5525. [[CrossRef](#)]
47. Xia, J.; Di, J.; Li, H.; Xu, H.; Li, H.; Guo, S. Ionic liquid-induced strategy for carbon quantum dots/bio(x = Br, Cl) hybrid nanosheets with superior visible light driven photocatalysis. *Appl. Catal. B Environ.* **2016**, *181*, 260. [[CrossRef](#)]
48. Abdel, K.A.M.; Fadlallah, S.A. Fabrication of titanium nanotubes array: Phase structure, hydrophilic properties, and electrochemical behavior approach. *J. Appl. Electrochem.* **2022**, *52*, 17. [[CrossRef](#)]
49. Wang, Y.; Yang, W.; Chen, X.; Wang, J.; Zhu, Y. Photocatalytic activity enhancement of core-shell structure g-C<sub>3</sub>N<sub>4</sub>@TiO<sub>2</sub> via controlled ultrathin g-C<sub>3</sub>N<sub>4</sub> layer. *Appl. Catal. B Environ.* **2018**, *220*, 337. [[CrossRef](#)]
50. Sun, X.Y.; Zhang, X.; Qian, N.X.; Wang, M.; Ma, Y.-Q. Improved adsorption and degradation performance by S-doping of (001)-TiO<sub>2</sub>. *Beilstein J. Nanotechnol.* **2019**, *10*, 2116. [[CrossRef](#)]
51. Rej, S.; Bisetto, M.; Naldoni, A.; Fornasiero, P. Well-defined Cu<sub>2</sub>O photocatalysts for solar fuels and chemicals. *J. Mater. Chem. A* **2021**, *9*, 5915. [[CrossRef](#)]
52. Rafiee, E.; Noori, E.; Zinatizadeh, A.A.; Zanganeh, H. A new visible driven nanocomposite including Ti-substituted polyoxometalate/TiO<sub>2</sub>: Synthesis, characterization, photodegradation of azo dye process optimization by RSM and specific removal rate calculations. *J. Mater. Sci.-Mater. Electron.* **2018**, *29*, 20668. [[CrossRef](#)]
53. Peng, X.; Wang, M.; Hu, F.; Qiu, F.; Zhang, T.; Dai, H.; Cao, Z. Multipath fabrication of hierarchical CuAl layered double hydroxide/carbon fiber composites for the degradation of ammonia nitrogen. *J. Environ. Manag.* **2018**, *220*, 173. [[CrossRef](#)] [[PubMed](#)]
54. Li, H.; Cao, Y.; Liu, P.; Li, Y.; Zhou, A.; Ye, F.; Xue, S.; Yue, X. Ammonia-nitrogen removal from water with g-C<sub>3</sub>N<sub>4</sub>-rGO-TiO<sub>2</sub> Z-scheme system via photocatalytic nitrification denitrification process. *Environ. Res.* **2022**, *205*, 112434. [[CrossRef](#)]
55. Sun, D.; Sun, W.; Yang, W.; Li, Q.; Shang, J.K. Efficient photocatalytic removal of aqueous NH<sub>4</sub><sup>+</sup>-NH<sub>3</sub> by palladium-modified nitrogen-doped titanium oxide nanoparticles under visible light illumination, even in weak alkaline solutions. *Chem. Eng. J.* **2015**, *264*, 728. [[CrossRef](#)]